

# Deep Learning Methods for Device Identification Using Symbols Trace Plot

Da Huang, *Graduate Student Member, IEEE*, Akram Al-Hourani, *Senior Member, IEEE*, Kandeepan Sithamparanathan, *Senior Member, IEEE*, and Wayne S.T. Rowe, *Member, IEEE*

**Abstract**—Devices authentication is one crucial aspect of any communication system. Recently, the physical layer approach radio frequency (RF) fingerprinting has gained increased interest as it provides an extra layer of security without requiring additional components. In this work, we propose an RF fingerprinting based transmitter authentication approach density trace plot (DTP) to exploit device-identifiable fingerprints. By considering IQ imbalance solely as the feature source, DTP can efficiently extract device-identifiable fingerprints from symbol transition trajectories and density center drifts. In total, three DTP modalities based on constellation, eye and phase traces are respectively generated and tested against three deep learning classifiers: the 2D-CNN, 2D-CNN+biLSTM and 3D-CNN. The feasibility of these DTP and classifier pairs is verified using a practical dataset collected from the ADALM-PLUTO software-defined radios (SDRs).

**Index Terms**—physical layer security, device authentication, RF fingerprinting, IQ imbalance, deep learning

## I. INTRODUCTION

Transmitter authentication has long been a significant task of communication security. Conventionally, popular device authentication algorithms such as challenge-handshake authentication protocol (CHAP) [1] and cryptography-based algorithms [2] are mainly software-based. Given their complexity, these algorithms are less realistic to implement on resource-limited systems. Physical layer authentication, however, is a potential alternative for low-complexity authentications. Early works already introduced simple physical layer level measurements such as round trip time (RTT) [3] and received signal strength indication (RSSI) [4] for device authentication. In some more recent works, such as artificial ambient environment (AAE) [5] and contextual co-presence based zero-interaction authentication (CCZIA) [6], sensors are introduced to provide extra information in assisting authentication. However, as the performance of the aforementioned approaches is highly restricted by the availability and precision of the utilized hardware, they potentially end up demanding rather high-end hardware at extra cost [7].

Recently, emerging research interests have been placed on a novel physical layer approach named radio frequency (RF) fingerprinting. Unlike approaches that use credentials, RF fingerprinting obtains device-identifiable fingerprints directly from the behavior of the hardware. As such, it benefits from

the capability of authenticating a device directly without needing extra components, hence a feasible candidate for low-cost and resource-constrained systems. Based on the characteristics used to generate the fingerprints, the existing RF fingerprinting approaches can be categorized into either channel- or signal-based approaches. The channel-based approaches use characteristics such as RSSI or channel state information (CSI) [8] to estimate and authenticate the device's location. The signal-based approaches extract device-identifiable fingerprints based on the unique hardware imperfections of each device. While channel-based approaches are good at tracking a device's presence variation (e.g. distance, angle and relative velocity), they require continuous measurement to maintain good performance and may perform poorly for applications without a specific localization setup. Due to such limitations, the remaining work focuses exclusively on signal-based RF fingerprinting, which is a more generalized option.

This work explores the feasibility of utilizing IQ imbalance *solely* as the source of device-identifiable fingerprints. We propose a novel signal representation approach, namely the density trace plot (DTP), to exploit fingerprints from the captured signal. The DTP can manifest symbols' transition trajectory and occurrence (density) on the same plot. Considering three types of DTPs, we explore the feasibility of utilizing 2D and 3D neural networks as classifiers for authentication. To the authors' best knowledge, it is the first work applying 3D neural networks to density plots for transmitter authentication.

To summarize, the main contribution of this work includes:

- We present a framework that utilizes IQ imbalance *solely* as the source of physical layer fingerprints for transmitter identification.
- We propose the density trace plot (DTP) for signal representation. We consider three formats: constellation DTP, phase DTP and eye DTP.
- We test all types of DTPs against three different deep learning architectures. Specifically, we consider the 2D-CNN, 3D-CNN and 2D-CNN+biLSTM in this work.
- We evaluate the performance of our proposed method using off-the-shelf ADALM-PLUTO SDRs under both wired and wireless conditions.

The rest of the paper is structured as follows: Section II conducts a review of relevant literature. Section III presents the system framework and the proposed DTP method. Section IV details the utilized practical setup and data collection procedure. Section V evaluates and discusses the performance of the proposed approach, and Section VI concludes the work.

\*Corresponding authors: D. Huang and A. Al-Hourani, E-mail: da.huang@ieee.org, akram.hourani@rmit.edu.au. Authors are with the School of Engineering, RMIT University, Melbourne, VIC 3000. This research received grant funding from the Australian Government under the Automotive Engineering Graduate Program.

## II. RELATED WORK

In signal-based RF fingerprinting, the device fingerprints are cultivated from the so-called physical layer impairments. Due to imperfection effects, including but not limited to device aging or manufacturing errors, each device experiences unique impairments along its lifespan. The impact of these intrinsic impairments is a random but device-independent process, thus yielding unique device-identifiable fingerprints. In relevant works, both a signal's transient and steady state segments are used to generate fingerprints. The transient-based approaches focus on the transmitted signal's short turn-on/off segment. This segment does not carry any actual data and only reflects the unique performance of the electronics. After obtaining the transient, features like energy spectral coefficients [9] and higher order statistical (HOS) such as instantaneous profiles, skewness and kurtosis [10], [11] are calculated and used to authenticate the transmitter accordingly. However, given the short duration of the transient segment, it requires a highly sensitive and well-synchronized receiver to capture the segment accurately. Due to this limitation, acquiring transient-related fingerprints in practice might be difficult. On the other hand, the steady state signal is easier to obtain. Although statistical measurements [12] remain a feasible option for steady state fingerprints, relevant studies tend to utilize specific RF impairments as the fingerprint sources. In a typical transceiver, the phase noise (PN), carrier frequency offset (CFO), IQ imbalance [13] and power amplifier (PA) imperfections [14], [15] are usually considered as possible sources of device-identifiable fingerprints.

Among all the impairments, we particularly focus on the IQ imbalance, a modulation domain impairment. In [16], the estimated IQ imbalance coefficients from a generalized likelihood ratio test (GLRT) estimator are used in a whitelist-based authentication method to detect transmitter relays. As argued by the authors, since IQ imbalance estimation and compensation is already a typical module in many off-the-shelf receivers, it is cost-efficient to utilize the estimation results for authentication. Using an industrial setup, the authors in [17] explore transmitter authentication using OQPSK signals collected from ZigBee devices. Each pre-processed input sequence is projected into four complex quadrant sequences, and a fingerprint vector with a total dimension of 72 is constructed from the new sequences. The fingerprint vectors are then used in a multiple discriminant analysis and maximum likelihood (MDA/ML) model to achieve authentication. In other literature, the IQ imbalance is often considered jointly with other impairments to form fingerprints. In [18], the raw received OQPSK signal is compared to its corrected version (i.e. impairments are estimated and compensated). An error vector is generated from the comparison and then used by a Gaussian Mixture Model (GMM) classifier to classify transmitters. According to the authors, impairments contributing to the performance include IQ imbalance, DC offset, CFO and PA non-linearity. In [19], OFDM signals that contain IQ imbalance, DC offset, carrier phase offset (CPO) and CFO are fed into a 2-channel 1D-CNN. Called the ORACLE, the CNN outputs a binary sequence for each input. The output

sequence is then compared to a whitelist-based matching table to identify the transmitters.

Apart from approaches that present numerical presentations to the classifier, some works explore image-based approaches. A constellation-based presentation approach, namely the differential constellation trace figure (DCTF), is proposed in a series of works as seen in [20]–[22]. A new sequence is first generated through a differential process between the original raw sequence and its time-delayed and conjugated copy. The DCTF is then obtained by projecting the new sequence into a 2D heatmap-like constellation map. As argued by the authors, the differential process converts the CFO into a fixed parameter; hence no further pre-processing is required. Under such an assumption, the potential fingerprint sources in the newly generated sequence include DC offset, IQ imbalance and the stabilized CFO. For best performance, manually selected time delay interval and IQ phase mismatch are intentionally injected into the conjugated copy before the differential process. In [20], [22], numerical features such as the DCTF cluster centers are obtained and are used in k-NN and SVM to achieve classification. While in [21], the 2D DCTF images are directly used to train 2D-CNNs. While DCTF-related works focus primarily on LoRa and ZigBee signals, a similar approach is proposed in [23] that focuses on OFDM signals from WiFi cards. The proposed differential contour stellar images are generated as three-channel RGB images by applying the same differential and projection process described above. The images are then used in a three-channel 2D-CNN to achieve authentication. Similarly, an intentional delay interval and IQ phase mismatch are required before the differential process. In [24], an IQ contour plot generated based on a 2D histogram is proposed to authenticate 4-QAM alike modulated samples from various satellite transmitters. However, the authors claim 10,000 IQ samples are used to generate a single image representation for best performance, which is less realistic for generic commercial communication systems. Focusing only on the WiFi preambles, authors in [25] convert the received OFDM signals into vectors of complex Gabor coefficients. All possible impairments after the CFO compensation are considered jointly to form the fingerprints within the coefficient vectors. Further in [26], the phase angles of the coefficient vectors are projected into 2D matrices and are used in a 2D-CNN.

As previously reviewed, traditional learning techniques such as the MDA/ML [12], [17] and conventional machine learning techniques SVM [10], [12] and k-NN [22] are widely adopted as the classifiers. However, as the physical layer impairments usually interact with each other in a non-linear manner, manual extraction of decisive RF fingerprints precisely is challenging. Owing to the capability to automatically extract features with minimum manual interaction, deep learning classifiers rise as one of the state-of-art solutions for many recent works [27]. The 1D-CNN is commonly used to handle sequence inputs like the raw or processed IQ sequence [28], [29]. For 2D representations such as images, 2D-CNNs are commonly used instead. For example, 2D-CNNs are introduced to classify time-frequency spectrogram generated using short-time Fourier transform (STFT) [28],

[30], continuous wavelet transform (CWT) or General Linear Chirplet transform [31]. Additionally, the modulation domain images DCTF [21] and the differential contour stellar [23] mentioned earlier also show decent compatibility with 2D-CNN. Noteworthy that authors in [32] start introducing 3D-CNN to handle stacked scatter images generated from a spatio-temporal helical representation. Besides CNNs, some works also take advantage of other deep learning architectures. For example, the long short-term memory (LSTM) network is a good alternative when handling time series, and is usually introduced to handle raw IQ sequences [28].

Contrary to a few reviewed image-based methods, such as [23], [24], that use colored images or images with relatively large sizes, our approach only considers single-channel grayscale images with a smaller size. Compared to other methods such as DCTF [21] that consider IQ imbalance, CFO and DC offset together as combined fingerprints, our approach considers IQ imbalance solely for authentication while no additional processing such as differential is required. Moreover, most methods only consider fingerprints presented within the constellation plane, while we also explore the possibility within the phase and time domain.

### III. METHODOLOGY

In typical direct conversion systems, the local oscillator and the following PA generate a set of orthogonal sine and cosine waves to up/down convert the in-phase (I) and quadrature (Q) channel signals. Ideally, the two orthogonal waves have the same frequency for transmitters and receivers. Whereas, due to the local oscillator imperfections, impairments such as CFO, CPO and IQ imbalance are introduced during the transmission. The IQ imbalance, specifically, refers to a gain and phase mismatch between the orthogonal wave pair as a combined effect of oscillator and PA imperfection [19]. Systems affected by such impairment consequentially causes the I and Q channel signals to lose orthogonality.

Since we only consider IQ imbalance as the targeting physical layer impairment, the captured signal undergoes several typical processing blocks within an RF receiver to isolate the targeting effect. It is beneficial in practice as no additional blocks need to be introduced for extra processing. Furthermore, as only the modulated waveform is of interest, the demodulation and decoding of bits are not required and hence are not presented in our system model.

#### A. Overall System Model

The overall system model diagram is shown in Fig. 1, indicating both the transmitter (device under test) and the receiver (detector device). The modules within the dotted line boxes represent architectures embedded in the hardware of an ADALM-PLUTO SDR.

At the transmitter end, the representation of a continuous IQ signal can be expressed as follows

$$x(t) = x_i(t) + jx_q(t), \quad (1)$$

where  $x_i(t)$  and  $x_q(t)$  are the modulated I and Q channel respectively. Accordingly, an ideal bandpass signal out of the transmitter is given by

$$y_{tx}(t) = \Re\{x(t)e^{i2\pi f_c t}\} = x_i(t)\cos(2\pi f_c t) - x_q(t)\sin(2\pi f_c t), \quad (2)$$

where  $f_c$  is the carrier frequency generated by the local oscillator. Due to imperfect carrier signals generated and amplified by the physical hardware, the I and Q branches suffer from unequal amplitude and phase. When taking the signal of the I channel as the reference, we denote the relative amplitude gain as  $\alpha$  and the relative phase difference as  $\phi$ , which are associated with the Q signal. In such manners, an imbalanced RF analytical bandpass signal out of the transmitter is represented as

$$y'_{tx}(t) = x_i(t)\cos(2\pi f_c t) - \alpha x_q(t)\sin(2\pi f_c t + \phi). \quad (3)$$

Without loss of generality, here we consider an ideal channel with a unity gain and zero phase shift. We also take a unity gain amplifier in both the transmitters and the receivers. Accordingly, the received bandpass signal is given as  $y_{rx}(t) = y'_{tx}(t)$ . In a typical SDR-based receiver, the imperfections of the receiver's oscillator introduce additional impairments during the down-conversion process, manifested as the CPO  $\theta$ , the CFO  $\delta f = f_{ctx} - f_{crx}$ . The  $f_{ctx}$  and  $f_{crx}$  respectively stand for the transmitter and receiver carrier frequency, and the amplitude mismatch  $\beta$  and phase mismatch  $\psi$  describe the receiver's IQ imbalance. Consequently, the baseband signals  $x_{ibb}$  and  $x_{qbb}$  are respectively given in (4) and (5) considering the impairments as per mentioned. The two signals are then filtered using a low-pass filter (LPF) to remove high frequency components, which further gives  $\hat{x}_i$ ,  $\hat{x}_q$  in (6) and (7) respectively. Finally, the discrete baseband analytical signal out of the receiver hardware is given as,

$$\hat{x}[n] = \hat{x}_i(nT_s) - j\hat{x}_q(nT_s), \quad (8)$$

where  $T_s$  is the sampling interval. Accordingly, the phase of the baseband analytical signal is given by,

$$\begin{aligned} \hat{\Phi}[n] &= \text{atan2}(\Im\{\hat{x}[n]\}, \Re\{\hat{x}[n]\}) \\ &= \text{atan2}(-\hat{x}_q(nT_s), \hat{x}_i(nT_s)), \end{aligned} \quad (9)$$

where  $\text{atan2}$  is the two-argument form of the arctan function, which allows  $[0, 2\pi)$  phase shift.

#### B. Signal Pre-processing

The discrete sequence  $\hat{x}[n]$  firstly passes through a few pre-processing blocks to eliminate impairments except for IQ imbalance. Impairments to be compensated include CFO, CPO and DC offset. We present our used methods for reproducibility purposes, and we acknowledge there might be other methods that can be utilized to achieve similar results. In fact, many off-the-shelf chipsets come with embedded pre-processing modules, and one can retrieve the required source sequences from which easily.

Due to the propagation along the transmission, the received signal might come in with various power losses and be affected by the channel. An option to start with is to remove the DC

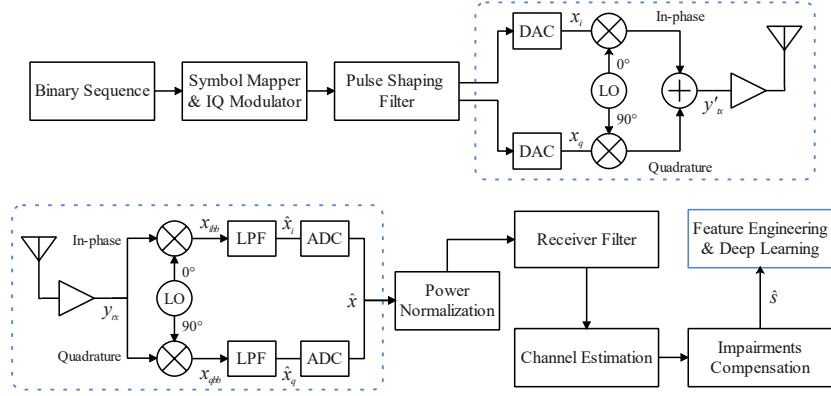


Fig. 1. System model diagram of the proposed direct conversion single carrier system framework.

$$\begin{aligned}
 x_{\text{ibb}}(t) &= y_{\text{rx}}(t)\cos(2\pi f_{\text{crx}}t + \theta) \\
 &= \frac{x_i(t)}{2} [\cos(2\pi(2f_{\text{crx}} + \delta f)t + \theta) + \cos(2\pi\delta ft - \theta)] \\
 &\quad - \frac{\alpha}{2}x_q(t) [\sin(2\pi(2f_{\text{crx}} + \delta f)t + \phi + \theta) + \sin(2\pi\delta ft + \phi - \theta)]. \tag{4}
 \end{aligned}$$

$$\begin{aligned}
 x_{\text{qbb}}(t) &= y_{\text{rx}}(t)\beta\sin(2\pi f_{\text{crx}}t + \psi + \theta) \\
 &= \frac{\beta}{2}x_i(t) [-\sin(2\pi(2f_{\text{crx}} + \delta f)t + \psi + \theta) + \sin(2\pi\delta ft - \psi - \theta)] \\
 &\quad + \frac{\alpha\beta}{2}x_q(t) [\cos(2\pi(2f_{\text{crx}} + \delta f)t + \phi + \psi + \theta) - \cos(2\pi\delta ft + \phi - \psi - \theta)]. \tag{5}
 \end{aligned}$$

$$\hat{x}_i(t) = \frac{x_i(t)}{2}\cos(2\pi\delta ft - \theta) - \frac{\alpha}{2}x_q(t)\sin(2\pi\delta ft + \phi - \theta). \tag{6}$$

$$\hat{x}_q(t) = \frac{\beta}{2}x_i(t)\sin(2\pi\delta ft - \psi - \theta) - \frac{\alpha\beta}{2}x_q(t)\cos(2\pi\delta ft + \phi - \psi - \theta). \tag{7}$$

offset and then normalize the samples to the average power of the received frame. This provides a unity power and avoids introducing biases in the classifier based on the signal power. Accordingly, we introduce a typical square-root raised-cosine (SRRC) filter for pulse shaping. The purpose of the filtering is to minimize inter-symbol interference (ISI). Lastly, we introduce the least mean square (LMS) algorithm for channel estimation. The LMS only compensates for channel effects and will not alter for other impairments of interest.

Accordingly, a few other techniques are utilized to compensate the unwanted impairments. The FFT-based coarse CFO compensation is conducted using the method proposed in [33]. For a sequence of length  $N_s$ , the estimation resolution is given as  $\omega_r = 2\pi/N_s$ . Since the transmitter and receiver are not synchronized, the targeted signal may only appear as part of a received frame. A matched filter is constructed based on a known reference sequence  $s_{\text{ref}}$  and is used to locate the starting and ending index of the actual signal. More detail of  $s_{\text{ref}}$  is covered in Section IV-B. The resulting sequence obtained from frame synchronization is denoted as  $s_{\text{FS}}$ . Further, the carrier synchronization block conducts a fine CFO and CPO compensation. In this work, the fine compensation is a two-step process. Firstly, a bank of matched filters is constructed

based on phase-shifted  $s_{\text{ref}}$ . The impulse response of the filter bank is given as

$$h_{\text{MF}}^{\Theta}[n] = \overline{s_{\text{ref}}[N_{\text{ref}} - n + 1]e^{j\Theta}}, \quad \Theta \in [-\pi, \pi), \tag{10}$$

where  $N_{\text{ref}}$  is the length of the reference sequence. After passing the sequence  $s_{\text{FS}}$  through the filter bank, the filter that returns the largest absolute convolution output is selected, and the corresponding  $\Theta$  is obtained as the estimated CPO. The compensated sequence  $s_{\text{CS}}[n]$  after the first step is denoted as

$$s_{\text{CS}}[n] = s_{\text{FS}}[n]\exp\left(-j \arg\max_{\Theta} |(s_{\text{FS}} * h_{\text{MF}}^{\Theta})[k]|\right). \tag{11}$$

The precision of the first step is largely affected by the selected steps of  $\Theta$ . Accordingly, the second step introduces a conjugate product estimator (CPE) [34] for a finer compensation to remove residual CPO and CFO.

As the proposed method has no interest in the actual data within the signal, no further processing is required. The final

discrete analytical signal  $\hat{s}[n]$  for authentication is given as

$$\hat{s}[n] = \frac{x_i(nT_s)}{2} - \frac{\alpha}{2}x_q(nT_s)\sin(\phi) + j \left[ \frac{\beta}{2}x_i(nT_s)\sin(\psi) + \frac{\alpha\beta}{2}x_q(nT_s)\cos(\phi - \psi) \right]. \quad (12)$$

### C. Feature Engineering

In this work, we convert the pre-processed sequence  $\hat{s}[n]$  into *trace plots* for better feature representation. A continuous trace plot can typically be obtained by connecting the discrete data points within the up-sampled discrete sequence. Compared to the discrete scatter plot, a continuous trace plot is better at visualizing transitions between adjacent symbols and spreading it spatially in a graph. As the trace plot is simply a remapping of the source sequence, the impairments presented in (12) remains in the generated plots and hence embrace device-identifiable fingerprints.

To exploit fingerprints due to IQ imbalance, we consider the following typical trace types:

**Type 1: Constellation trace.** The constellation trace plot is a typical technique to showcase the transition between consecutive symbols within the IQ plane. Given the imbalanced amplitude and phase between the two channels, the IQ imbalance changes steady state symbol locations. As a result, significant IQ imbalance results in a squeezed and tilted constellation view.

**Type 2: Eye trace.** The trace within an eye diagram highlights the time domain transition between adjacent symbols. This approach visualizes the impacts of IQ imbalance from the time domain point of view. The IQ imbalance potentially affects a few characteristics of an eye trace plot. For instance, the imbalanced amplitude leads to different eye heights and eye amplitude between the I and Q channels. Moreover, the out-of-sync phase leads to potential shifts in the jitter and the rise and fall time when the eye plots of the two channels are compared together.

**Type 3: Phase trace.** As calculated following (9), the phase of an IQ imbalanced signal also embeds potential fingerprints. Based on an observation from the constellation view, the IQ imbalance leads to varied symbol positions. When reflected in the phase plane, such variation leads to potential shifts in the concentration of one or more phase states.

Examples of the three introduced trace representations generated from an emulated 4-QAM signal are shown in Fig. 2. The time domain waveform is first normalized to achieve a normalized amplitude between [-1,1] for both channels. The phase and eye trace plots are plotted across normalized symbol time axes that cover two symbol duration.

The typical trace plots explained above are good at statistically manifesting the steady states of a modulated signal. However, the generated plots become messy and overcrowded as the length of the source sequence increases. The overcrowded plots rather result in reduced fingerprints for the classifier. To overcome this issue, we propose a novel representation

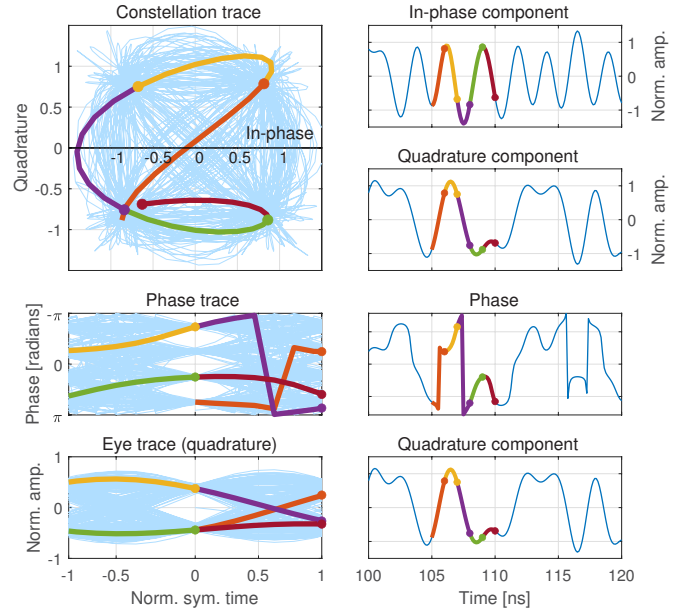


Fig. 2. Light blue lines show the whole IQ trajectory of a 4-QAM sample, while the colored segments highlight the trajectories of five randomly selected consecutive symbols.

approach, namely the density trace plot (DTP), in this work. Contrary to the traditional trace plots that only present spatial transition trajectories between symbols, the proposed approach can simultaneously capture symbols' density (i.e., occurrence). By introducing the density as extra information, the DTP highlights the concentration centers of the original sequence within different domains, making it easier for the classifier to detect any drifts from the steady states.

In typical communication systems, the received signals are sampled as discrete data points located around specific symbol locations. To recover the transition trajectories between adjacent symbols, we upsample the received  $\hat{s}[n]$  by ten times. We find this number sufficient to generate adequate traces while avoiding significant memory consumption. To further exploit any density-related information, we map the upsampled sequence into a bivariate histogram plot of width (number of columns)  $w$  and height (number of rows)  $h$ . The bivariate histogram groups the data into 2-D bins and records the number of data points that fall into a certain bin. That is, for arbitrary data point  $(x_p, y_p)$ , it falls into bin  $b_{r,c}$  of the bivariate histogram if it satisfies both

$$x_p \in [x_{\lim}^{(r,c)}, x_{\lim}^{(r,c+1)}), \quad y_p \in [y_{\lim}^{(r,c)}, y_{\lim}^{(r+1,c)}] \quad (13)$$

where  $r \in [1, h]$  and  $c \in [1, w]$ , while  $x_{\lim}^{(r,c)}$  and  $y_{\lim}^{(r,c)}$  are the lower bounds of bin  $b_{r,c}$ . More specifically, the lower bin bounds are obtained as

$$x_{\lim}^{(r,c)} = x_{\min} + \frac{|x_{\max} - x_{\min}|(c-1)}{w} \quad (14)$$

and

$$y_{\lim}^{(r,c)} = y_{\min} + \frac{|y_{\max} - y_{\min}|(r-1)}{h}, \quad (15)$$

where  $[x_{\min}, x_{\max}]$  and  $[y_{\min}, y_{\max}]$  are the minimum and maximum possible values of  $(x_p, y_p)$ . To prevent extremely high

bin values from dominating the resulting plot, bin values  $v_{r,c}$  of all  $b_{r,c}$  are converted into log-scale and normalized into a range of  $[0, 255]$ , so that it yields 8-bit unsigned integer and satisfies the pixel values for a grayscale image in general. That is, for arbitrary  $v_{r,c}$ , it is normalized to

$$v_{r,c} = \begin{cases} \left\lceil \frac{255 \times \log_{10}(v_{r,c})}{\log_{10}(\max(v_{r,c}))} \right\rceil, & \text{if } v_{r,c} \neq 0 \\ 0, & \text{if } v_{r,c} = 0 \end{cases}, \quad (16)$$

where  $\max(v_{r,c})$  denotes finding the global maximum value among all possible  $v_{r,c}$ .

Example DTPs of different types of trace plots are shown in Fig. 3. To better illustrate how three utilized DTPs capture the impact of IQ imbalance, DTPs generated from samples injected with an arbitrary amount of IQ imbalance are further given in Fig. 3(b). Notice that the examples are plotted using scaled pseudo color only for visualization purposes, while all data entries are stored as single channel 8-bit integers as calculated in (16). As a special case, the eye DTP of I and Q channels are generated separately and then concatenated to form a two-channel integer-valued matrix. That is, the dimension remains  $[h \times w \times 1]$  for constellation DTP (Type 1) and phase DTP (Type 3), an eye DTP (Type 2) has a dimension of  $[h \times w \times 2]$ . The selection of  $h$  and  $w$  affects the bin numbers of a DTP frame, which further affect the amount of learnable feature. The impact of these parameters is discussed later in section IV-D. Indeed, a modulation scheme's complexity (e.g., modulation order) also affects the resulting DTPs. For instance, as presented in Fig 4, the constellation (Type 1) DTPs of different modulation schemes have various density concentrations and are assumed to embrace corresponding fingerprints.

Like the examples presented in Fig. 3 and Fig. 4, the whole sequence yields a single DTP. This scenario is further denoted as 2D-DTP, as illustrated in Fig. 5. This approach projects all temporal variations into spatial 2D representations akin to capturing a moving object with a long exposure camera shot. As such, 2D-DTP might not consider potential temporal features. As an alternative, the same signal sequence is chopped into  $N_f$  frames (segments), and a 2D-DTP is generated per segment. All the frames generated from the same source sequence are stacked together to form an image sequence. As shown in Fig. 6, this approach is denoted as the 3D-DTP accordingly. Therefore, the dimensions of the image sequence become  $[h \times w \times N_f \times 1]$  for constellation DTP and phase DTP, while  $[h \times w \times N_f \times 2]$  for the eye DTP. Similarly, the selection of  $N_f$  might affect the performance of the 3D-DTP, which is further discussed in Section IV-D.

#### D. Classifier

Since we consider both 2D and 3D presentations, we utilize three different deep learning networks respectively to handle DTPs of various dimensions.

1) *2D-CNN*: CNN is a feed-forward deep learning algorithm and is an efficient tool for image-based classification tasks. A custom-designed 2D-CNN, similar to the one proposed and verified in our previous work [30], is introduced to

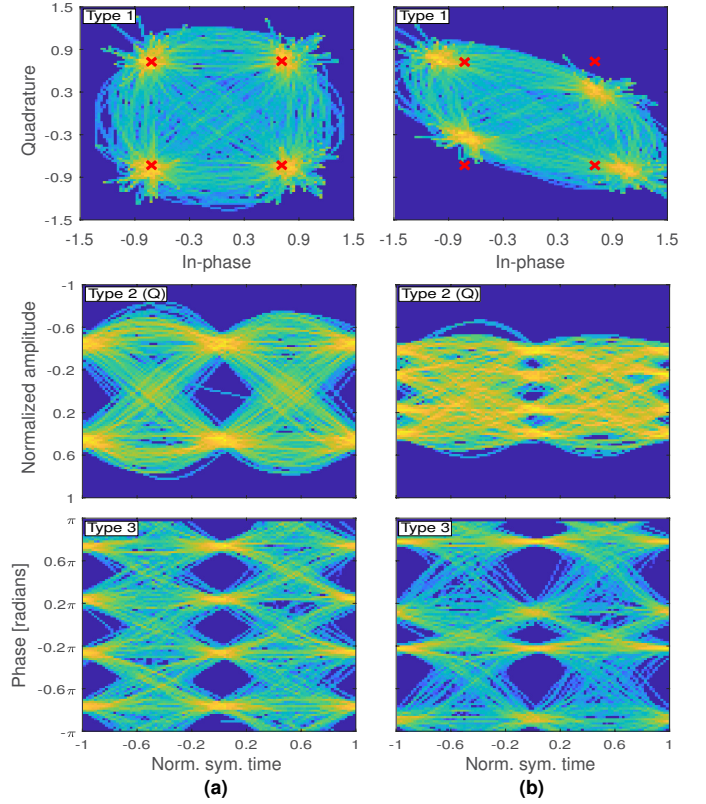


Fig. 3. Examples of the constellation (Type 1), eye (Type 2, Q channel only) and phase (Type 3) 2D-DTPs of a 4-QAM sample, with SNR = 10 dB. Column (a) presents DTPs generated from the original sample, and (b) presents DTPs generated from the same sample injected with IQ imbalance. The red crosses in the constellation view indicate the ideal symbol positions.

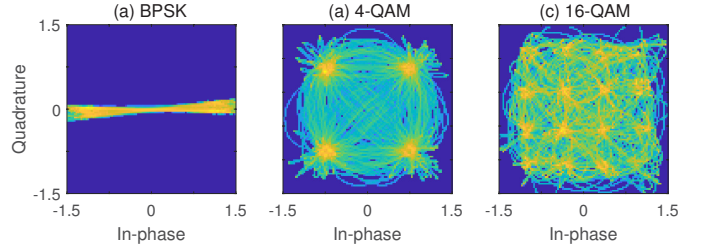


Fig. 4. Example constellation (Type 1) DTPs of different modulation schemes, of which source sequences are 500 symbols long for both.

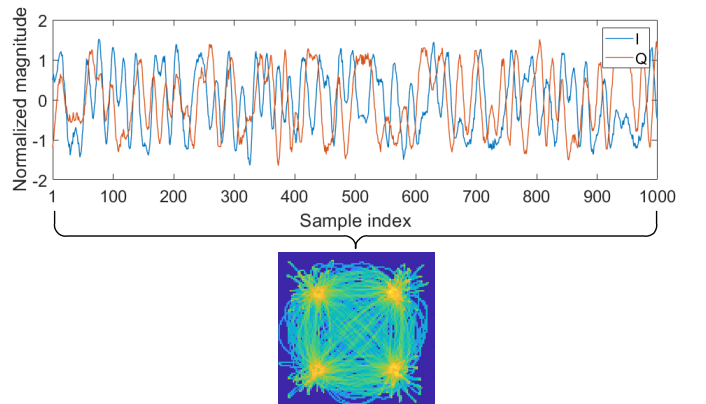


Fig. 5. Example of constellation (Type 1) 2D-DTP generated from a 4-QAM sample, with SNR = 10 dB.

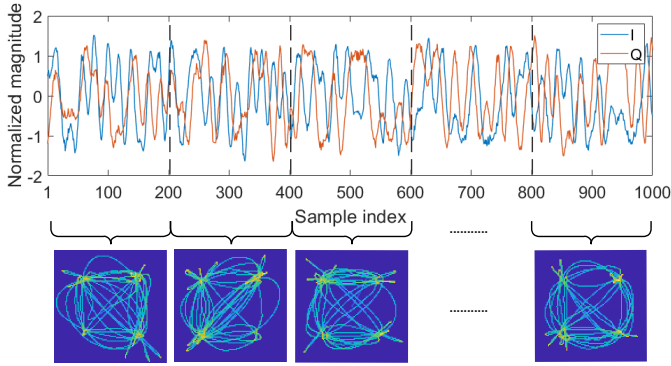


Fig. 6. Example of constituting constellation (Type 1) 3D-DTP using a sequence of 2D-DTP frames from a 4-QAM sample, with SNR = 10 dB.

handle 2D-DTP inputs. Unlike the previously used architecture, we add batch normalization layers between each convolutional and activation layer. Batch normalization aims to adjust the learned feature map to maintain a standard distribution, increasing the trained network's generality and robustness. As shown in Fig. 7(a), the network has a multi-stage architecture, where the number of convolutional blocks  $n_b$  blocks could be dynamically adjusted for balanced performance between accuracy and processing time. Each convolutional block consists of two 2D convolutional layers to extract potential features, followed by one max-pooling layer to limit the dimensions of the inputs.

2) *2D-CNN+biLSTM*: The 2D-CNN only handles 2D image inputs. Thus additional networks are designed to make the most of the temporal features from 3D-DTP sequences. Inspired by the network proposed in [35], an LSTM network is integrated with the 2D-CNN to achieve a hybrid architecture. Different from [35], we concatenate a bidirectional long short time memory (biLSTM) block to the 2D-CNN as in Fig. 7(b). The biLSTM network is a particular form of LSTM that can learn an input sequence in both forward and backward directions. Compared to the conventional LSTM, a biLSTM usually provides a more accurate prediction when complete sequences are available. As the 3D-DTP sequences are always generated using the entire  $\hat{s}[n]$ , hence are suitable for biLSTM. In the 2D-CNN+biLSTM architecture, the CNN network process each frame of the input 3D-DTP sequence one by one, flattening and stacking the learned activations after the last max-pooling layer. This process yields a feature matrix with dimensions of  $[N_{ac} \times N_f]$ , where  $N_{ac}$  is the number of activations output by the last max-pooling layer. This intermediate feature matrix used as input for biLSTM is regarded as a time series block that consists of  $N_f$  time points and  $N_{ac}$  learnable features per time point.

3) *3D-CNN*: As an alternative, a 3D-CNN is also utilized in this work to handle 3D-DTP sequences. As presented in Fig. 7(c), a 3D-CNN has a similar architecture to the 2D-CNN, while the 3D convolutional layers replace the 2D ones. The 3D-CNN takes the whole 3D-DTP sequence at once, requiring large memory to store and process the data batch. To prevent possible memory depletion, an extra max-pooling layer is added after the first 3D convolutional layer in all the

blocks to reduce the feature maps' size steeply.

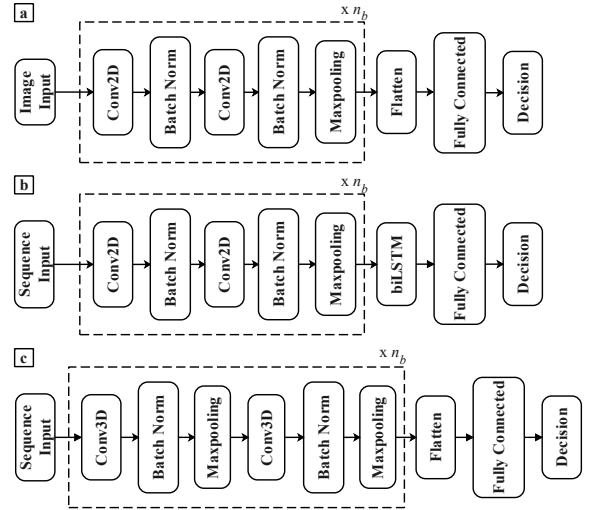


Fig. 7. Example architectures of three utilized deep learning networks: (a) 2D-CNN, (b) 2D-CNN+biLSTM and (c) 3D-CNN.

#### IV. EXPERIMENTAL SETUP AND DATA HANDLING

##### A. Practical Hardware Setup

We utilize the commercially available ADALM-PLUTO SDR as both the transmitter and receiver device for the experimental hardware setup. Compared to other off-the-shelf modules, this specific hardware is selected because it grants us more control of the transmitted signals and the status of embedded modules. Five SDRs are utilized as transmitters, and an additional SDR is consistently used as the receiver. To test the feasibility of the proposed method, we start with a wired connection by connecting the transmitter SDR to the receiver SDR directly using an RF cable, as shown in Fig. 8(a). The purpose of the step is to minimize the impact of the wireless channel and only focus on the variations brought by the physical layer impairments. Moreover, we collected data over-the-air to test our method in a more realistic environment. Similar to the example illustrated in Fig. 8(b), we consider the scenario where the transmitters and the receiver are placed in the same room and at an approximate distance of 1.5 meters. The channel in this setup can be regarded as a Rician channel given the presence of the line of sight (LoS) path.



Fig. 8. Experimental hardware setup contains the utilized transmitters (Txs) and receiver (Rx). Examples of (a) a wired connection and (b) an over-the-air channel.

Both the transmitter and receiver are connected to the same PC but controlled by separate MATLAB instances to allow parallel operation. The auto gain controller (AGC) is disabled on devices of both ends, and the gain is manually selected so that the ideal average received power gives 0 dBm. Additionally, noticed in [36], on the receiver end, potential flicker noise occurs around DC, i.e., 0Hz, thus to avoid operating near the center of the baseband spectrum, a frequency shifts  $f_{cs}$  is applied to the transmitter so that  $f_{ctx} = f_c + f_{cs}$  to minimize the impact of such flicker noise. The  $f_{cs}$  is removed at the receiver before further processing.

Lastly, a few assumptions and measurements are made to limit the variations. As it may take approximately one year to observe obvious alternations in the oscillator, such as more than 10ppb of frequency drifts in the local oscillator [37], we assume constant impairments for all tested devices. Under this assumption,  $\beta$  and  $\psi$  in (12) remain constant when consistently using the same receiver SDR, and hence only the relative impairments from the transmitter (with respect to the receiver) are considered. As IQ imbalance is found to be sensitive against chip heating [38], the ambient temperature of the test environment is monitored to avoid the potential noise introduced due to varying temperatures.

### B. Dataset Generation

In this work, all transmitted signals are modulated using the quadrature amplitude modulation (QAM) scheme. In total, we consider BPSK (equivalent to 2-QAM), 4-QAM, 16-QAM and 64-QAM at a symbol rate of  $R_{sym} = 1$  Msym/s. Noteworthy we only include 64-QAM in over-the-air testing to investigate the stability of our approach across different modulation scales. The transmitted signals are generated as 500-symbol-long for all modulation schemes, which we found adequate to carry sufficient fingerprints while not resulting in a significant computational burden. Sequence generation for each modulation scheme is independent and pseudo-randomly. To prevent sequence patterns from causing fingerprint variations, the generation is made as a one-off process, i.e., the same generated sequences are reused throughout the study. Moreover, the ideal modulated sequences (after pulse shaping) are stored separately as  $s_{ref}$  and are used as the reference sequence during matched filtering. The data transmission follows the system framework in Fig. 1 and the hardware setup in Fig. 8.

The wired dataset is collected across five consecutive days, where samples collected from day one to day four are used for training, while samples collected on day five are only used to test trained networks. During the first four days, approximately 2,500 samples per modulation type per transmitter are collected through the wired connection. On the fifth day, 500 samples are collected for each transmitter and each modulation scheme. The over-the-air dataset is collected separately across four additional days. In total, approximately 2,000 samples per modulation per transmitter are collected wirelessly. As a result, we collected a dataset comprising around 85,000 samples in total. To observe the behavior of the framework under different noise power, during the signal processing phase, MATLAB is used to measure and inject a controlled additive white

Gaussian noise (AWGN) into the received signal such that we can emulate SNR levels ranging from -20 dB to 20 dB.

### C. Training

To fully evaluate the potential of the proposed method, we test three utilized deep learning classifiers against all DTP types. That is, we consider all nine possible combinations for each modulation scheme. Among the whole dataset, a random portion of 80% is selected as *training* set, and the remaining 20% is set aside as the *testing* set, which is not involved in the training process. Within the *training* set, the data is randomly divided into three splits and are used for k-fold verification (i.e. one split performs as the *validation* set each time). The training set only consists of samples with SNRs of -10 dB, 0 dB and 10 dB, while samples in the testing set cover the tested SNR range. As DTPs of each modulation might embody different fingerprints presentation and require various network designs, networks for each possible combination are independently trained. Considering three modulation schemes with nine possible combinations per modulation, 27 networks are independently trained and optimized.

All the processing and training are conducted using MATLAB on the PC with Intel Core i7 10700KF CPU and one NVIDIA RTX GeForce 2070s GPU. During the training of each network, the stochastic gradient descent with momentum (SGDM) is utilized as the solver and a Bayesian optimization based parameter sweep is applied to find its optimal hyperparameters. The particular hyperparameters to be tuned during the training include the number of convolutional blocks  $n_b$ , the kernel size and filter numbers for each convolutional layer, as well as the number of hidden units for the biLSTM block. We set a maximum of 200 iterations for each optimization round and 30 epochs per training iteration. Upon finishing, the network that returns the highest validation accuracy is selected as the final product. Overall, we find the networks achieved a balance between performance and computational complexity when having  $n_b = 2$ . Due to the large number of trained networks, presenting all their hyperparameters at once is less meaningful. Instead, we summarize the major hyperparameters of each modulation scheme's best-performed network in Table II. Please refer to Section V for more details on selecting these networks.

### D. Parameters

As mentioned in previous sections, the bin numbers (image size)  $[h, w]$  of a 2D-DTP, as well as the frame numbers  $N_f$  of a 3D-DTP sequence, potentially affect the DTP's capability to exploit fingerprints. The selection of  $[h, w]$  impacts the number of total bins in a DTP. A DTP is more likely to manifest concentrated density centers and show more distinguishable transition trajectories with larger bin numbers. For 3D-DTP, when having a source sequence with fixed length  $N_s$ , different frame numbers  $N_f$  lead to varying symbols-per-frame (symbols/frame). As illustrated in Fig. 9, each frame manifests clearer density centers with higher symbols/frame, i.e., smaller  $N_f$ . Another assumption is made that both  $N_f$

and symbols/frame affect the learnable features, and there is a trade-off between the two parameters.

In order to get more insight into this trade-off, a subset of 4-QAM samples from all five transmitter SDRs is selected for a preliminary trial. For simplicity, only samples at SNR=10 dB are used, and only the constellation (Type 1) DTP is used for the trial. A bank of 2D-DTPs with various sizes is first generated. Again, for simplicity, we set  $h = w$  for all generated DTPs. Following the same training manner described in the section above, several 2D-CNNs that take different input sizes are trained. The performance of these networks is measured using the interquartile range (IQR) and the average classification accuracy as in Fig. 10(a). Based on the results, we select  $h = w = 100$  for a balance between performance and complexity, given that no significant increment of accuracy is observed beyond this point. After determining the  $[h, w]$ , a bank of 2D-CNN+biLSTM networks is trained using 3D-DTP sequences generated with varying symbols/frame. The performance of these networks is again presented in IQR and average classification accuracy as in Fig. 10(b). We select 50 symbols/frame for the best performance based on the observation. Given the fixed sequence length used in this work, this selection corresponds to  $N_f = 10$ . Despite the preliminary trial only being conducted on a limited scale, the selection of parameters is applied to all studied DTP types and modulation schemes.

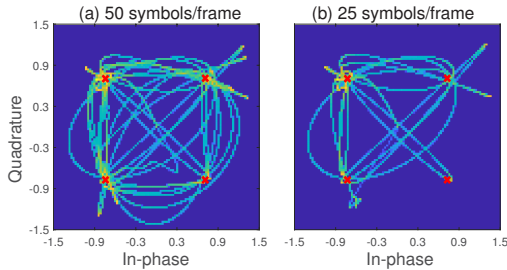


Fig. 9. Example of constellation (Type 1) 3D-DTP frames of a 4-QAM sample generated with different symbols-per-frame: (a) 50 symbols/ frame, and (b) 25 symbols/ frame. All examples are with  $h = w = 100$ . The red crosses indicate the ideal position of each symbol.

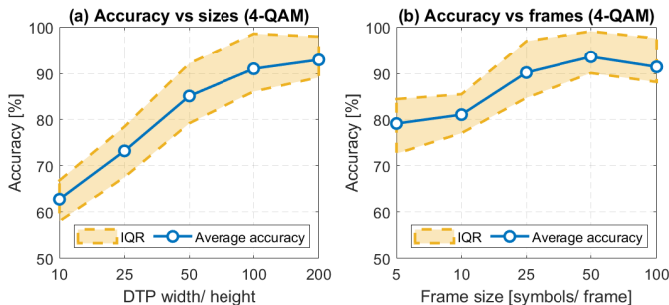


Fig. 10. Performance of 2D-DTPs with different dimensions (SNR=10 dB).

Values of key parameters that are used in data transmission and DTP generation are summarized in Table I, while the hyperparameters of each modulation scheme's best-performed network are summarized in Table II. Every entry of Table II follows the following format:  $[kernel\ width \times kernel\ height]$

- *filter numbers*. The approximate total learnable of each network is also provided considering five classes.

TABLE I  
PARAMETERS TABLE

Parameter	Symbol	Quantity
Carrier frequency	$f_c$	2.5 [GHz]
Carrier frequency shift	$f_{cs}$	1 [MHz]
Sampling frequency	$f_s$	8 [MHz]
Symbol rate	$R_{sym}$	1 [Msymbols/s]
Samples per symbol <sup>1</sup>	sps	8
DTP width (column number)	w	100
DTP height (row number)	h	100
Number of frames <sup>2</sup>	$N_f$	10
Number of convolutional blocks	$n_b$	2
Length of transmitted sequence	$N_s$	500
Length of reference sequence <sup>3</sup>	$N_{ref}$	4000

<sup>1</sup> For pulse shaping filter.

<sup>2</sup> For 3D-DTP generation, when having 50 symbols-per-frame.

<sup>3</sup>  $N_{ref} = N_s \times sps$ .

TABLE II  
HYPERPARAMETERS FOR BEST-PERFORMED CNNs

Layers	Hyperparameters			
	BPSK	4QAM	16QAM	64QAM
conv_1_1	[8×8]-22	[5×5]-25	[7×7]-24	[7×7]-24
conv_1_2	[8×8]-22	[5×5]-25	[7×7]-24	[7×7]-24
maxpool_1	[2×2]	[2×2]	[2×2]	[2×2]
conv_2_1	[4×4]-11	[4×4]-7	[4×4]-27	[7×7]-23
conv_2_2	[4×4]-11	[4×4]-7	[4×4]-27	[7×7]-23
maxpool_2	[2×2]	[2×2]	[2×2]	[2×2]
Approx. total learnables	41k	21.7k	58.3k	88.2k

## V. RESULTS AND DISCUSSIONS

### A. Behavior under Wired Transmission Link

The performance of all possible DTP and deep learning classifier pairs are verified. We select the average classification accuracy at SNR=10 dB as a metric and plot the result of all 27 scenarios as a heatmap in Fig. 11. Among all the tested pairs, the Type 1 2D-DTP achieves the highest overall average accuracy for all tested modulation schemes. The other two DTP types perform well in most combinations, despite major failures observed in Type 2 for BPSK and Type 3 for 16-QAM. Confusion matrices of all scenarios at SNR=10 dB are plotted in Fig. 12 and Fig. 13 to better visualize the device-wise classification performance. The results show transmitter No.3 (Tx3) shows a higher chance of misclassification, such as in Type 2 3D-DTP with 3D-CNN pair of 4-QAM. These outliers might result from less significant device-identifiable fingerprints that failed to be learned by the network.

An SNR sweep is applied to the best-performed pair of each modulation scheme to observe the impact of noise power. Additionally, we compare the performance of our approach against the DCTF methods [21]. DCTF representations of the same size are generated from the same dataset and trained using networks as summarized in Table II. In the sweep results presented in Fig. 14, the accuracy maintains a proportional relationship with the SNR before it saturates at around SNR=10 dB. This result is consistent with our previous

		BPSK			4-QAM			16-QAM		
DTP types	Con.	88.41	78.02	68.49	96.72	86.18	90.39	92.71	82.52	81.79
	Ph.	81.74	62.95	55.6	93.15	73.97	83	22.97	23.98	26.17
	Eye	31.72	23.3	23.3	93.79	82	57.82	90.79	86.52	73.12
		2D-CNN	biLSTM	3D-CNN	2D-CNN	biLSTM	3D-CNN	2D-CNN	biLSTM	3D-CNN

Deep learning algorithms

Fig. 11. Classification accuracy (%) of constellation (Con.), phase (Ph.) and eye DTPs against different deep learning algorithms at SNR = 10 dB.

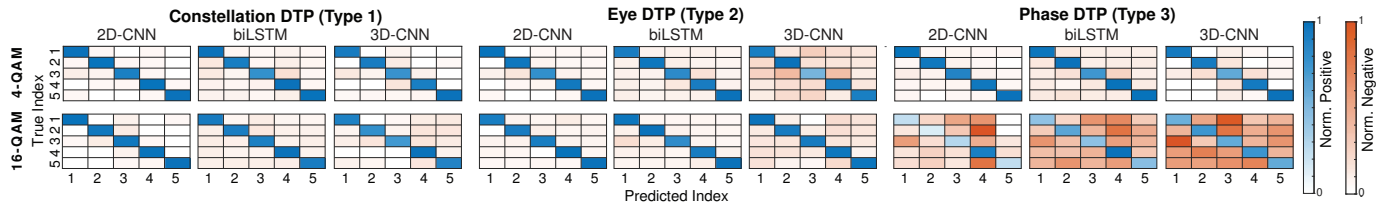


Fig. 12. Confusion matrices for different DTP and deep learning pairs at SNR = 10 dB. Matrices are color coded to showcase normalized positive rate and negative rate in different colors.

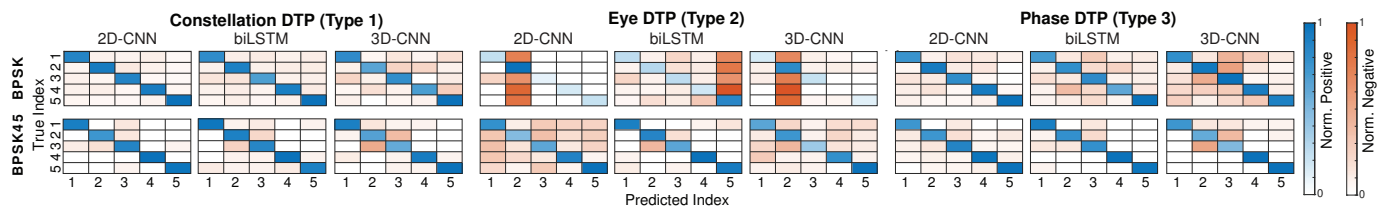


Fig. 13. Confusion matrices for different DTP and deep learning pairs at SNR = 10 dB. Matrices are color coded to showcase normalized positive rate and negative rate in different colors. The BPSK45 stands for phase-shifted BPSK.

work in [30]. Under the same testing condition, the DCTF method scored higher accuracy at low SNR regions. However, our methods achieve similar or better performance in high SNR regions, especially for schemes of higher modulation orders. Notice that as five transmitter devices are involved in the testing, the worst-scenario classification accuracy is 20% (i.e., 1/5).

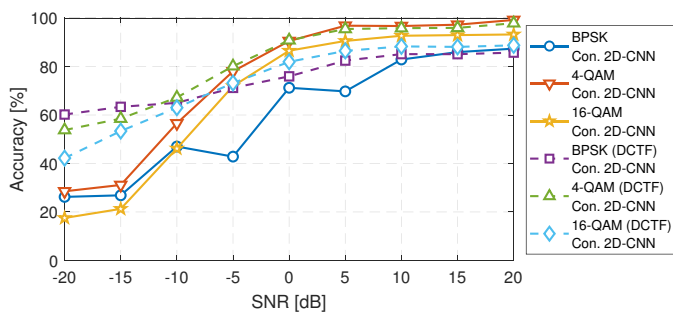


Fig. 14. SNR sweep of the best-performed DTP pairs for each modulation scheme.

As previously mentioned, Type 3 DTPs failed to produce acceptable results for 16-QAM. It is potentially due to a modulated 16-QAM signal having more phase states in its phase plane presentation, which leads to more ambiguity in any generated Type 3 DTPs. The results reveal a potential deficiency of the approach when applied to high-order modulation schemes. Given the fixed length of the transmitted sequence and the aim for equal symbol occurrence, each symbol is granted fewer occurrences as the modulation order grows.

It potentially causes the fingerprints not to be adequately expressed.

A sequence comprising 2000 symbols is generated for a preliminary trial to test this assumption. The purpose of having a longer sequence is to increase each symbol's occurrence. As shown in Fig. 15 (b), the phase DTP shows more concentrated density centers along each phase state. The newly generated DTPs are then used to train a new set of networks, of which results are presented Fig. 16. The matrices are row-normalized (i.e. respectively against the total observations of the corresponding true class) to visualize the *recall* of a specific class. Compared to previous results, the classification accuracy of the longer sequence is significantly improved.

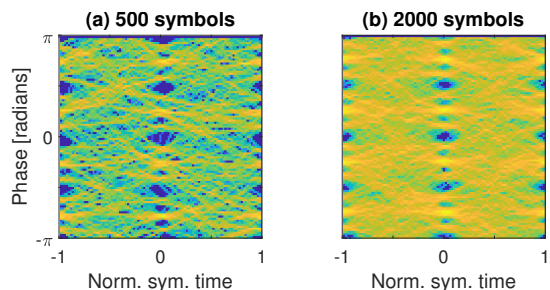


Fig. 15. 16-QAM phase 2D-DTP with SNR=10 dB generated when: (a) input sequence is 500 symbols long, and (b) input sequence is 2000 symbols long.

Similarly, the Type 2 DTPs failed to work with BPSK, while the Type 1 and Type 3 DTPs also achieved worse overall performance than other modulation schemes. A possible reason

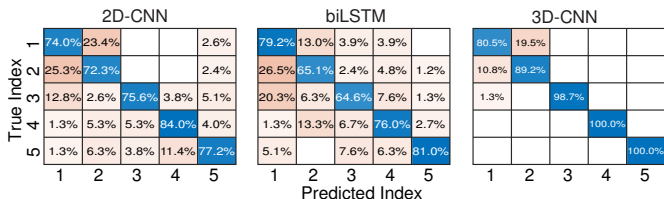


Fig. 16. Confusion matrices for 16-QAM phase DTPs with SNR=10 dB generated when the source sequence is 2000 symbols long.

is that the ideal BPSK signals encode no information on its quadrature channel, which gives  $x_q(t) = 0$  in (6) and (7). In such cases, the amount of learnable fingerprints is partially demolished, especially for the quadrature channel eye diagram, and left the deep learning algorithms with insufficient information. We attempt to generate and transmit BPSK signals with an additional 45 degrees phase shift to address this problem. The example 2D-DTPs of shifted BPSK are illustrated in Fig. 17. The collected phase-shifted BPSK samples are used for another preliminary trial. The classification results of these newly trained networks are presented in Fig. 18 and the second row of Fig. 13, where noteworthy improvements are observed.

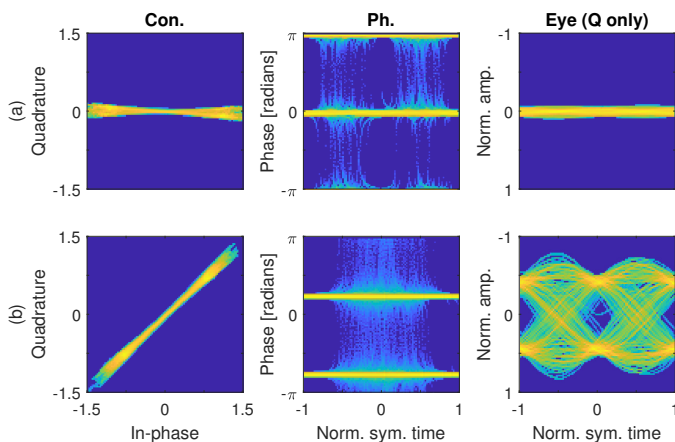


Fig. 17. Example 2D-DTPs of BPSK sample with SNR=10 dB: (a) without phase shift, and (b) with 45° phase shift.

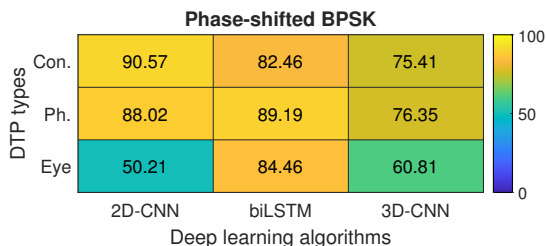


Fig. 18. Classification accuracy (%) of phase-shifted BPSK at SNR=10 dB.

It is worth mentioning that both of the preliminary trials are conducted using a subset only to investigate the possibility of the alternations. Comprehensive testing under such arrangements would be beneficial for future work.

## B. Behavior under Wireless Transmission Link

We further test the proposed framework against data collected over the air to evaluate its robustness. As mentioned previously, the utilized channel estimation algorithm does not alter the physical layer impairments. Thus the identical processing procedures described in Section III-B can be reused in this scenario.

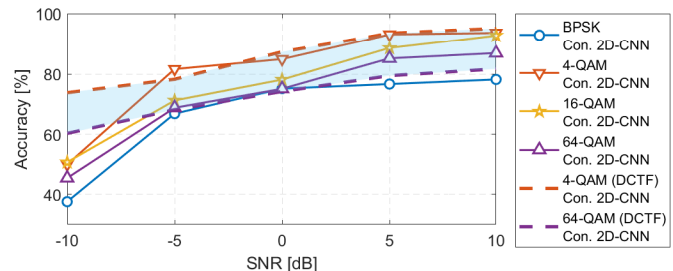


Fig. 19. SNR sweep of the best-performed DTP pairs for each modulation scheme under the presence of a Rician channel.

We start by involving 64-QAM samples and assuming the best performance is also achieved for Type 1 DTP with 2D-CNN. Using the same network setup as in Table II and following the same training manner, new networks for over-the-air samples are trained and validated. As the SNR sweep results presented in Fig. 19, the over-the-air scenario achieves a similar outcome compared to Fig. 14), despite slight drops in classification accuracy. Here we only present DCTF results of 4-QAM and 64-QAM for a less crowded plot. Nevertheless, the performance of other intermediate modulation schemes is found to fall within the shaded area. The DCTF again is more robust across the whole SNR range, however, our approach is found to achieve a higher positive rate for modulation of high orders.

Additionally, the performance of all the possible pairs of the 4-QAM modulation scheme is presented in Fig. 20 to evaluate the overall performance better. Overall, 2D-CNN achieves the highest accuracy for all three DTP types, yet the 2D-CNN+biLSTM architecture achieves the worst overall validation accuracy. The poor performance of 2D-CNN+biLSTM is potentially due to the training dataset failing to present possible scenarios comprehensively. As a form of RNN, the nature of the biLSTM block limits its capability of normalizing the feature distributions across time steps. Due to such limitation, a trained network is poorly performed if the inputs have varying distributions, such as under the stochastic time-varying channels.

## C. Discussions

Among all tested modulation schemes, the original BPSK performs worse than others when comparing the average performance across different modulation schemes. Given ideal BPSK modulates no data on its Q channel, such a relatively low complexity transition might partially reduce the detectable fingerprints caused by physical layer impairments. Introducing the extra phase shift leads to  $x_q(t) \neq 0$  in (12), which further results in increased impairments within the captured signals.

		2D-CNN					biLSTM					3D-CNN				
		<b>Constellation DTP (Type 1)</b>														
True Index	1	91.4%	1.7%	0.7%	3.3%	3.0%	70.0%	4.0%	1.0%	20.0%	5.0%	90.1%	1.7%	1.7%	2.4%	4.1%
	2	0.7%	93.2%		4.1%	2.0%	10.2%	81.6%	1.8%	4.7%	1.7%	0.3%	31.6%	3.1%	5.4%	9.5%
	3	0.3%	0.7%	97.6%	0.7%	0.7%	0.8%	7.0%	88.9%	2.7%	0.7%	2.4%	2.7%	90.8%	3.4%	0.7%
	4	3.4%	1.4%	0.3%	93.5%	1.4%	9.5%	5.7%	0.5%	84.2%	0.1%	11.8%	17.8%	2.4%	55.7%	12.2%
	5	2.7%	2.0%	0.3%	1.4%	93.6%	4.3%	0.9%	0.2%	7.5%	87.1%	10.3%	6.9%	4.8%	6.9%	71.1%
		<b>Eye DTP (Type 2)</b>														
True Index	1	94.5%	1.4%		2.7%	1.4%	80.4%	17.9%	4.6%	9.6%	7.5%	78.8%	7.5%	1.4%	5.5%	6.8%
	2	2.0%	94.9%	0.7%	1.7%	0.7%	0.3%	75.4%	5.4%	4.7%	14.2%	7.5%	79.0%	1.4%	7.1%	5.1%
	3	0.3%	0.3%	97.3%	1.4%	0.7%	0.1%	25.4%	71.0%	1.2%	2.3%	1.0%	1.4%	96.3%	1.0%	0.3%
	4	1.7%	2.1%	1.0%	93.4%	1.7%	0.6%	21.9%	1.0%	62.5%	13.9%	5.5%	3.5%	0.7%	86.5%	3.8%
	5	0.7%	1.0%			98.3%	0.1%	22.4%	0.8%	5.6%	71.1%	3.4%	3.7%	1.7%	1.7%	89.5%
		<b>Phase DTP (Type 3)</b>														
True Index	1	85.6%	4.8%	1.7%	4.5%	3.4%	40.2%	21.0%	3.7%		35.0%	94.2%	1.7%		2.7%	1.4%
	2	5.4%	84.7%	1.0%	7.1%	1.7%	6.5%	39.5%	6.3%		47.7%	3.8%	86.8%	1.5%	3.4%	4.5%
	3	0.3%	0.3%	95.3%	1.7%	1.7%	0.9%	18.4%	56.5%		14.2%	1.4%	1.4%	95.6%	0.7%	1.0%
	4	5.2%	5.2%	1.0%	86.5%	2.1%	1.9%	9.3%	2.2%	48.3%	38.2%	1.8%	1.4%		94.7%	2.1%
	5	5.4%	2.4%	1.0%	3.4%	87.8%	4.9%	11.3%	1.0%		82.8%	2.4%	0.3%		2.4%	94.9%
		1 2 3 4 5					1 2 3 4 5					1 2 3 4 5				
		Predicted Index														

Fig. 20. Confusion matrices (row-normalized) for networks trained and evaluated using over-the-air 4-QAM samples, tested at SNR=10 dB.

Similar observations for other modulation schemes indicate that a more diverse transition between symbols potentially contributes to increased learnable fingerprints. However, as the modulation order increases, it becomes more challenging to distinguish adjacent symbols within DTP of limited size. Thus, as a result, some degradation in authentication accuracy is observed as modulation complexity grows. Utilizing DTP of varying sizes might be a potential solution towards the problem.

Regarding the classification performance among the three proposed DTP types, the constellation DTP (Type 1) achieves the best overall performance. A possible reason is that we specifically focus on IQ imbalance as the only impairment in this work. As mainly a modulation domain impairment, the IQ imbalance leads to a tilted constellation view. Compared to the complex alternations in the eye diagram and the phase plane, the tilted constellation benefits from a more straightforward and distinguishable presentation. Nevertheless, test results still indicate excellent potential for eye DTP (Type 2) and phase DTP (Type 3) to function across different modulation schemes. A separate test utilizing those two DTP types for different impairment sources would be beneficial as a potential future work.

The two 3D networks perform slightly worse than the 2D-CNN when comparing three utilized deep learning approaches. It is potentially due to the limited temporal features available within a relatively short transmission duration. As in the long sequence trial as in Fig. 16, it is noticed the 3D networks start to outperform 2D-CNN when a longer sequence is transmitted. Also, limited by the available resource in this work, we can only iterate through certain hyperparameter settings of a 3D network, which might leave it not trained to the optimal. When only comparing the two 3D networks, as discussed in the previous section, the nature of the biLSTM block makes it

vulnerable to varying data distributions. As such, when the randomness of the channel becomes significant, the classification performance might be curbed. The 3D-CNN, on the other hand, produces a more solid performance, especially when handling data collected wirelessly owing to the utilization of batch normalization layers.

## VI. CONCLUSION

In this work, we proposed a novel signal representation approach DTP to identify RF transmitters based on their physical layer properties. The presented data modalities exploit hardware impairment IQ imbalance solely as the clue for identifying different transmitters. Presented using three different modalities, the proposed data representation can be handled with either 2D or 3D neural networks for more flexibility. The experimental results show the best-performed DTP and deep learning pair can accurately classify five transmitting devices with an overall classification accuracy of up to 96.7%.

This work serves as the validation of our method. Indeed we acknowledge there are a few limitations in the scope of this work that needs to be addressed in future work. For instance, investigation under a more complex environment (e.g. with more Tx devices, under the presence of an NLOS path or at a low SNR region) is necessary. Moreover, investigating the impact of source sequence patterns and lengths on the classification performance would also benefit future work.

## REFERENCES

- [1] W. Liang and W. Wang, "On performance analysis of challenge/response based authentication in wireless networks," *Computer Networks*, vol. 48, no. 2, pp. 267–288, 2005.
- [2] L. Marin, M. P. Pawlowski, and A. Jara, "Optimized ECC implementation for secure communication between heterogeneous IoT devices," *Sensors (Switzerland)*, vol. 15, no. 9, pp. 21 478–21 499, 2015.
- [3] S. Brands and D. Chaum, "Distance-Bounding Protocols," in *Advances in Cryptology — EUROCRYPT '93*, T. Hellese, Ed. Berlin, Heidelberg: Springer Berlin Heidelberg, 1994, pp. 344–359.
- [4] Y. Wu, K. Wang, Y. Sun, and Y. Ji, "R2NA: Received Signal Strength (RSS) Ratio-Based Node Authentication for Body Area Network," *Sensors*, vol. 13, no. 12, pp. 16 512–16 532, dec 2013. [Online]. Available: <http://www.mdpi.com/1424-8220/13/12/16512>
- [5] I. Gurulian, K. Markantonakis, E. Frank, and R. N. Akram, "Good Vibrations: Artificial Ambience-Based Relay Attack Detection," *Proceedings - 17th IEEE International Conference on Trust, Security and Privacy in Computing and Communications and 12th IEEE International Conference on Big Data Science and Engineering, Trustcom/BigDataSE 2018*, pp. 481–489, 2018.
- [6] M. Conti and C. Lal, "Context-based Co-presence detection techniques: A survey," *Computers and Security*, vol. 88, p. 101652, 2020.
- [7] I. Boureanu and S. Vaudenay, "Challenges in distance bounding," *IEEE Security and Privacy*, vol. 13, no. 1, pp. 41–48, 2015.
- [8] Z. Wang, W. Dou, M. Ma, X. Feng, Z. Huang, C. Zhang, Y. Guo, and D. Chen, "A Survey of User Authentication Based on Channel State Information," *Wireless Communications and Mobile Computing*, vol. 2021, pp. 1–16, 2021.
- [9] M. Kose, S. Tascioglu, and Z. Telatar, "RF Fingerprinting of IoT Devices Based on Transient Energy Spectrum," *IEEE Access*, vol. 7, pp. 18 715–18 726, 2019.
- [10] A. Aghnaiya, Y. Dalveren, and A. Kara, "On the performance of variational mode decomposition-based radio frequency fingerprinting of bluetooth devices," *Sensors (Switzerland)*, vol. 20, no. 6, 2020.
- [11] Y. Yang, A. Hu, and J. Yu, "A practical radio frequency fingerprinting scheme for mobile phones identification," *Physical Communication*, vol. 55, p. 101876, 2022.
- [12] X. Wang, Y. Zhang, H. Zhang, X. Wei, and G. Wang, "Identification and authentication for wireless transmission security based on RF-DNA fingerprint," *Eurasip Journal on Wireless Communications and Networking*, vol. 2019, no. 1, 2019.

- [13] A. Mohammadian and C. Tellambura, "RF Impairments in Wireless Transceivers: Phase Noise, CFO, and IQ Imbalance - A Survey," *IEEE Access*, vol. 9, pp. 111 718–111 791, 2021.
- [14] S. Dolatshahi, A. Polak, and D. L. Goeckel, "Identification of wireless users via power amplifier imperfections," *Conference Record - Asilomar Conference on Signals, Systems and Computers*, pp. 1553–1557, 2010.
- [15] Y. Li, Y. Ding, G. Goussetis, and J. Zhang, "Power Amplifier enabled RF Fingerprint Identification," *Proceedings of the 2021 IEEE Texas Symposium on Wireless and Microwave Circuits and Systems: Making Waves in Texas, WMCS 2021*, 2021.
- [16] P. Hao, X. Wang, and A. Behnad, "Amplify-and-forward relay identification using joint Tx/Rx I/Q imbalance-based device fingerprinting," *EURASIP Journal on Wireless Communications and Networking*, vol. 2019, no. 1, p. 64, 2019.
- [17] C. M. Rondeau, M. A. Temple, J. A. Betances, and C. M. Schubert Kabban, "Extending critical infrastructure element longevity using constellation-based ID verification," *Computers and Security*, vol. 100, pp. 1–26, 2021.
- [18] M. Pospíšil, R. Marsalek, and J. Pomenkova, "Wireless device authentication through transmitter imperfections - Measurement and classification," *IEEE International Symposium on Personal, Indoor and Mobile Radio Communications, PIMRC*, pp. 497–501, 2013.
- [19] K. Sankhe, M. Belgiovine, F. Zhou, L. Angioloni, F. Restuccia, S. D'Oro, T. Melodia, S. Ioannidis, and K. Chowdhury, "No Radio Left Behind: Radio Fingerprinting Through Deep Learning of Physical-Layer Hardware Impairments," *IEEE Transactions on Cognitive Communications and Networking*, vol. 6, no. 1, pp. 165–178, mar 2020.
- [20] Y. Jiang, L. Peng, A. Hu, S. Wang, Y. Huang, and L. Zhang, "Physical layer identification of LoRa devices using constellation trace figure," *Eurasip Journal on Wireless Communications and Networking*, vol. 2019, no. 1, 2019.
- [21] L. Peng, J. Zhang, M. Liu, and A. Hu, "Deep Learning Based RF Fingerprint Identification Using Differential Constellation Trace Figure," *IEEE Transactions on Vehicular Technology*, vol. 69, no. 1, pp. 1091–1095, Jan 2020.
- [22] Y. Yang, A. Hu, J. Yu, G. Li, and Z. Zhang, "Radio frequency fingerprint identification based on stream differential constellation trace figures," *Physical Communication*, vol. 49, p. 101458, 2021.
- [23] J. Li, Y. Ying, C. Ji, and B. Zhang, "Differential Contour Stellar-Based Radio Frequency Fingerprint Identification for Internet of Things," *IEEE Access*, vol. 9, no. April, pp. 53 745–53 753, 2021.
- [24] G. Oligeri, S. Sciancalepore, S. Raponi, and R. D. Pietro, "Past-ai: Physical-layer authentication of satellite transmitters via deep learning," *IEEE Transactions on Information Forensics and Security*, vol. 18, pp. 274–289, 2023.
- [25] M. K. Fadul, D. R. Reising, T. D. Loveless, and A. R. Ofoli, "RF-DNA Fingerprint Classification of OFDM Signals Using a Rayleigh Fading Channel Model," *IEEE Wireless Communications and Networking Conference, WCNC*, vol. 2019-April, 2019.
- [26] M. K. Fadul, D. R. Reising, and M. Sartipi, "Identification of OFDM-Based Radios under Rayleigh Fading Using RF-DNA and Deep Learning," *IEEE Access*, vol. 9, pp. 17 100–17 113, 2021.
- [27] A. Jagannath, J. Jagannath, and P. S. P. V. Kumar, "A comprehensive survey on radio frequency (RF) fingerprinting: Traditional approaches, deep learning, and open challenges," *Computer Networks*, vol. 219, no. November, p. 109455, 2022.
- [28] G. Shen, J. Zhang, A. Marshall, L. Peng, and X. Wang, "Radio Frequency Fingerprint Identification for LoRa Using Deep Learning," *IEEE Journal on Selected Areas in Communications*, vol. 39, no. 8, pp. 2604–2616, aug 2021.
- [29] T. Jian, B. C. Rendon, E. Ojuba, N. Soltani, Z. Wang, K. Sankhe, A. Gritsenko, J. Dy, K. Chowdhury, and S. Ioannidis, "Deep Learning for RF Fingerprinting: A Massive Experimental Study," *IEEE Internet of Things Magazine*, vol. 3, no. 1, pp. 50–57, 2020.
- [30] D. Huang, A. Al-Hourani, K. Sithamparanathan, W. S. T. Rowe, L. Bulot, and A. Thompson, "Deep learning methods for device authentication using rf fingerprinting," in *2021 15th International Conference on Signal Processing and Communication Systems (ICSPCS)*, 2021, pp. 1–7.
- [31] G. Baldini and C. Gentile, "Transient-Based Internet of Things Emitter Identification Using Convolutional Neural Networks and Optimized General Linear Chirplet Transform," *IEEE Communications Letters*, vol. 24, no. 7, pp. 1482–1486, 2020.
- [32] M. Ramasubramanian, C. Banerjee, D. Roy, E. Pasilio, and T. Mukherjee, "Exploiting Spatio-Temporal Properties of I/Q Signal Data Using 3D Convolution for RF Transmitter Identification," *IEEE Journal of Radio Frequency Identification*, vol. 5, no. 2, pp. 113–127, jun 2021.
- [33] Y. Wang, K. Shi, and E. Serpedin, "Non-data-aided feedforward carrier frequency offset estimators for QAM constellations: A nonlinear least-squares approach," *Eurasip Journal on Applied Signal Processing*, vol. 2004, no. 13, pp. 1993–2001, dec 2004.
- [34] Q. Chaudhari, *Wireless Communications from the Ground Up: An SDR Perspective*. CreateSpace Independent Publishing Platform, 2018.
- [35] S. Skaria, D. Huang, A. Al-Hourani, R. J. Evans, and M. Lech, "Deep-learning for hand-gesture recognition with simultaneous thermal and radar sensors," in *2020 IEEE SENSORS*, 2020, pp. 1–4.
- [36] A. Al-Hourani, R. J. Evans, P. M. Farrell, B. Moran, M. Martorella, S. Kandeepan, S. Skafidas, and U. Parampalli, "Chapter 7 - Millimeter-wave integrated radar systems and techniques," in *Academic Press Library in Signal Processing, Volume 7*, R. Chellappa and S. Theodoridis, Eds. Academic Press, 2018, pp. 317–363.
- [37] R. Filler and J. Vig, "Long-term aging of oscillators," *IEEE Transactions on Ultrasonics, Ferroelectrics and Frequency Control*, vol. 40, no. 4, pp. 387–394, Jul 1993.
- [38] M. Pospisil, R. Marsalek, and T. Gotthans, "Wireless device classification through transmitter imperfections - Evaluation of performance degradation due to the chip heating," *IEEE Radio and Wireless Symposium, RWS*, pp. 169–172, 2017.